Implementation of an analysis pipeline to evaluate quantitative mapping of multiple physical parameters in glioma patients

Jim Zhao

Bachelor's thesis

Implementation of an analysis pipeline to evaluate quantitative mapping of multiple physical parameters in glioma patients

Jim Zhao

04.03.2020

Institute for Data Processing
Technische Universität München

Jim Zhao. *Implementation of an analysis pipeline to evaluate quantitative mapping of multiple physical parameters in glioma patients.* Bachelor's thesis, Technische Universität München, Munich, Germany, 2020.

Supervised by Prof. Dr.-Ing. K. Diepold and PD Dr. C. Preibisch; submitted on 04.03.2020 to the Department of Electrical Engineering and Information Technology of the Technische Universität München.

Institute for Data Processing, Technische Universität München, 80290 München, Germany, http://www.ldv.ei.tum.de/.

Abstract

Glioma, one of the most common intracranial tumors, account for 81% of all malignant brain tumors. Although occuring rarely, they are often fatal.
In this work, an analysis pipeline was implemented in modular form to calculate quantitative maps of multiple physical parameters, including proton density PD, the transverse relaxation time T_2, and the longitudinal and effective transverse relaxation rates R_1 and R_2^*, respectively, from multiple MR images with different contrast weightings. The pipeline was implemented in MATLAB, partially utilizing existing toolboxes and frameworks. The pipeline was validated with data exported from the MR scanner directly and from the Picture Archiving and Communication System (PACS). Quantitative parameter maps of five healthy subjects were evaluated with different configuration settings and were validated by comparing the estimated parameter maps with values reported in literature. Lastly, the pipeline was used to analyse the quantitative values in eight postoperative glioma patients in five volumes of interest (VOI): The oedema surrounding the resected glioma, and the affected and non-affected hemisphere in both gray and white matter.
The results indicated a trend, that glioma also affect normal-appearing tissue on a global scale, because we observed a change of the physical parameters. However, the patient cohort was too small to draw conclusions. R_1 values in glioma patients in both gray and white matter could clearly be separated into two groups. These differences in R_1 values could resemble the progression of disease or different types of glioma. Further research is necessary to consolidate this assumption.

Contents

1 Introduction

In recent years, magnetic resonance imaging (MRI) has proved to be a favorable tool in clinical diagnosis. Due to technical improvements, both in scanner hardware and software, the scanning time of patients can be reduced to several minutes, while the resolution has consistently increased.
MRI is a non-invasive, real-time examination, which can routinely be applied for screenings. Compared to computer tomography (CT), MRI has no radiation and a higher contrast for soft tissue, making it ideal for examinations of the abdomen, the thorax, or the brain among others. Furthermore, MRI has proved to be the most sensitive modality for the detection of primary or recurrent breast cancer [17].
Although it is still discussed how the "value" of MRI in a clinical setting should be measured correctly, MRI can be undoubtedly seen as one of the most powerful tools in modern clinical diagnosis, providing multimodal information on metabolism, function and structure [40]. Besides its application in diagnosis, MRI is also used to guide minimal-invasive surgeries or to prognose the mortality of diseases. Moreover, its use was extended to many other fields, including functional MRI, fiber tracking in neuroradiology or quantitative MRI in precision medicine [40].
Quantitative MRI quantifies physical properties of the tissue, such as relaxation times or rates, proton density, or magnetic susceptibility and has greatly improved the specificity and sensitivity in computational neuroanatomy [45]. The specific physical parameters can also be used as biomarkers for structural changes caused by disease, which remain unseen in conventional MRI [26].
Another recently emerging field related to quantitative MRI is the so-called histological MRI (hMRI). Microstructural brain tissue parameters, such as myelin density or axonal diameters, which could previously only be obtained with ex-vivo histology, were derived in-vivo from conventional MRI using biophysical models [4]. Thus, state-of-the-art MRI techniques proved to be a non-invasive and fast method for histological analyses.
Glioma are one of the most common brain tumors and account for $81\,\%$ of all malignant brain tumors. Although they occur rarely, they cause significant mortality. For instance, Glioblastoma , which make up around $45\,\%$ of all gliomas, have a 5-year relative survival of barely $5\,\%$ [27]. In a recent study, multimodal MRI was used to predict the WHO grade of glioma based on machine learning algorithms [48]. This study suggests, that tumor biology is reflected in multimodal MRI information, which can non-invasively be evaluated through MR to improve diagnosis and treatment.

Recent improvements in image analysis in MRI, such as automatic brain tumor segmentation, progression assessment and survival prediction using machine learning algorithms [3], often require large computational resources which are often not available in the clinical environment.
Data processing pipelines are a way to smoothly integrate research results into clinical routine to improve diagnosis and treatment. These pipelines connect the MR scanner with a server with sufficient computation power, which analyses the acquired data and sends the results back to the scanner. By doing so, costs can be reduced, as there is no need to upgrade every scanner with higher computing power. Additionally, maintenance is easier, since updates can be carried out remotely at the server.
In this work, an analysis pipeline was implemented, which calculates quantitative maps from conventional MR images. This pipeline is then used to analyse multiple physical parameters in glioma patients. It ensures reproducibility and is less prone to error, as the calculation of quantitative maps is very fragmented.
In the *Fundamentals* section, technical and medical fundamentals concerning MR imaging are presented. Subsequently, the *Methods* section covers the methods used in this work. Thereafter, in the *Results* section the results are presented. The results are discussed in the subsequent *Discussion* section. Finally, the work finishes with a *Conclusion*.

2 Fundamentals

The discovery of the Nuclear Magnetic Resonance (NMR) effect by Bloch and Purcell in 1946, laid the ground to the development of Magnetic Resonance Imaging (MRI) [5][33]. In 1973 the first image based on NMR was acquired by Lauterbur [20]. Since then, the imaging quality of MRI has improved considerably, in particular due to better hardware, higher computing power and improved postprocessing. These days, an isotropic resolution of $1\,\mathrm{mm}^3$ or less is commonly achieved in clinical imaging. In the following sections, some background concerning the physical and technical principles as well as medical fundamentals and clinical applications are presented.

2.1 Technical Fundamentals

2.1.1 Image generation

In order to understand how images are generated with MRI in general, the underlying physical principals are explained in the following subsections.

Signal creation

The fundamental physical property underlying every MRI technique is the quantum mechanic property of a spin. Nuclei with non-zero spin have both an angular moment and a magnetic moment. In clinical MRI, the most common target is the proton of the ${}^1H$ isotope, which has spin equal to $\frac{1}{2}$. From a macroscopic, simplified view, nuclei with non-zero spin can be interpreted as small dipoles, which, if placed in a strong static magnetic field with field strength B_0, align parallel or anti-parallel to the direction of B_0. In a collection of nuclei, the so-called spin ensemble, slightly more nuclei align parallel to the magnetic field, which results in a small net magnetization. A radiofrequency (RF) pulse is necessary to tilt the net magnetization away from B_0 and the nuclei become phase coherent. The longer the RF pulse is applied, the larger the angle α between the direction of B_0 and the net magnetization, which is often referred to as the flip angle. The nuclei tilted away from the direction of B_0 precess about B_0 with the so-called resonance or Lamor frequency ω_0, which is described by the equation $\omega_0 = \gamma \cdot B_0$ with the gyromagnetic ratio γ.
Now, the magnetic vector also possesses a transverse component, precessing about B_0, which induces a measurable voltage signal in the receive coils. If the

RF pulse is removed, two processes take place at the same time: The nuclei begin to dephase and simultaneously return to their original parallel or anti-parallel orientation. The longitudinal relaxation process is characterized by the time constant T_1, while the transverse dephasing is characterized by the time constants of the intrinsic relaxation T_2 and the effective transverse relaxation T_2^*. Transverse dephasing takes place due to two different reasons. Firstly, microscopic spin-spin interactions cause the spins to dephase. Also, static inhomogenities of the external magnetic field B_0 contribute to additional dephasing. T_2 characterizes the transversal dephasing resulting only from the former effect, while T_2^* characterizes dephasing resulting from both effects [43]. While it is possible to measure T_2^* with gradient echo sequences, spin echo sequences can be used to avoid measuring effects from static inhomogeneities, such that it is possible to obtain T_2. Both types of sequences will be explained in the next sections.
The strength of the received signal depends on the transverse or the longitudinal relaxation, as well as the proton density (PD).

Spatial coding with magnetic field gradients

Now, the question arises how spatial information is encoded, such that structural information can be obtained from these measurements.
In the simplest case of multi-slice 2D imaging, a linear magnetic gradient is first created, which decreases in strength along one axis. Thus, the protons in each layer along the gradient direction experience different magnetic field strengths and according to the Lamor equation also have a different precession frequency depending on their position. Therefore, by choosing the frequency of the so-called slice selection RF pulse accordingly, only the protons in the corresponding slice will be excited. The slice excited by the RF pulse is encoded along the remaining two dimensions with a so-called frequency-encoding magnetic gradient and a phase-encoding magnetic gradient. The frequency-encoding gradient is turned on along one axis during read-out. This gradient changes the strength of the magnetic field, which causes the protons in the slice to precess with different frequencies along the direction of the gradient. As the protons along the gradient direction precess with different frequencies, their positions can be reconstructed by decomposing the contributions of the different frequencies. Similarly, the last dimension is encoded with a phase-encoding magnetic gradient. However, signal contributions with the same frequency, but with different phases can not be differentiated in the Fourier spectrum. The trick is to apply multiple phase-encoding steps at different gradient strengths and measure the dephased signals. Since measuring a dephased signal is actually equivalent to sampling the signal over time, the rate of change, i.e. its frequency, can be again analyzed with the Fourier Transform.
To understand, how the spatial information within the slice is encoded, the concept of Fourier Transformation is required. Essentially, the Fourier Transformation can be

understood as a method to derive the contributions of any frequency to a given signal. A mathematical more profound explanation can be found in the next subsection. In conclusion, by analyzing the frequencies and phases of the measured signal with 2D Fourier Transformation, the image can be reconstructed.

Image Reconstruction

The final step now left, is to reconstruct the MRI image from the received signal S. The measured signals described in the previous subsection are equivalent to data points $\mathbf{k}_n \in D$ in the so-called k-space, which is also known as the frequency spectrum, where D is the set of sampled k-space points. The k-space points $\mathbf{k}_n$ in the rectilinear sampling case, assuming frequency encoding along the x-axis and phase encoding along the y-axis, are defined as:

$$\mathbf{k}_n = a \cdot \Delta k_x + b \cdot \Delta k_y, \quad a, b = ..., -2, -1, 0, 1, 2... \tag{2.1}$$

with

$$\begin{cases} \Delta k_x = \gamma |G_x| \, \Delta t \\ \Delta k_y = \gamma \Delta G_y T_{pe} \end{cases} \tag{2.2}$$

where G_x is the frequency-encoding gradient, Δt is the readout sampling time interval, ΔG_y is the phase-encoding gradient step size and T_{pe} is the phase-encoding interval. Mathematically, the reconstruction problem can be formulated as follows: Find the image $I(r)$, given

$$S(k_n) = \int I(r) e^{-i2\pi k_n \cdot r} dr \tag{2.3}$$

Since the multidimensional Fourier transform is separable into multiple one-dimensional Fourier transforms, we only need to consider the one-dimensional case here. For uniformly sampled data

$$D = \{k_n = n\Delta k, n = ..., -2, -1, 0, 1, 2, ...\} \tag{2.4}$$

the imaging equation becomes

$$S[n] = S(n\Delta k) = \int_{-\infty}^{+\infty} I(x) e^{-i2\pi n \Delta k x} dx. \tag{2.5}$$

An important formula proven in [21], describes how to reconstruct $I(x)$ from $S(n\Delta k)$:

$$\sum_{n=-\infty}^{\infty} S[n] e^{i2\pi n \Delta k x} = \frac{1}{\Delta k} \sum_{n=-\infty}^{\infty} I(x - \frac{n}{\Delta k}) \tag{2.6}$$

In the ideal case of infinite sampling, which means that infinite data points $\mathbf{k}_n$ were measured, the image can be completely reconstructed as long as the sampling satisfies the Nyquist sampling criterion. It states that an image $I(x)$ of finite dimension, i.e. there is a W_x such that $I(x) = 0$ for $|x| > W_x/2$, can be reconstructed uniquely, if the relationship $W_x < 1/\Delta k$ is fulfilled.
Then the image $I(x)$ can be simply reconstructed with following infinite Fourier series

$$I(x) = \Delta k \sum_{n=-\infty}^{\infty} S[n] e^{i2\pi n \Delta k x}, |x| < \frac{1}{\Delta k}. \tag{2.7}$$

However, in practice an infinite sampling is not feasible. In finite sampling the Fourier series becomes truncated and is often referred to as the "Fourier reconstruction formula":

$$I(x) = \Delta k \sum_{n=-N/2}^{N/2-1} S[n] e^{i2\pi n \Delta k x}, |x| < \frac{1}{\Delta k}, \tag{2.8}$$

where $N + 1$ is the number of sampling points
Note that the image reconstructed through finite sampling does not represent the imaged object perfectly, since the truncation of the sum has led to a loss of information.

2.1.2 Basic Pulse Sequences

In the following subsections, two pulse sequences are presented, which are the basis for most pulse sequences.
By manipulating imaging parameters, such as the repetition time (TR) and the echo time (TE) accordingly, it is possible to weigh the contributions of the physical parameters T_1, T_2, T_2^* and PD to the final contrast. TR refers to the time period between two excitation pulses, while TE is the time interval between application of the excitation pulse and the measurement of the MR signal. T_1-weighted images, i.e. images, where T_1 influences the final contrast the most, can be achieved with short TR and short TE, T_2-weighted images can be acquired with long TR and long TE and PD-weighted images can be acquired with long TR and short TE.

Spin Echo Sequences

In spin echo (SE) sequences (see Figure 2.1), the slice-selective 90° RF pulse is followed by a 180° RF pulse after the time interval TE/2 to refocus the spins, which have dephased after the application of the 90° RF pulse. Due to the static inhomogenities of B_0, the spins precess with a slightly different Lamor frequency and start to dephase. By applying the 180° pulse, the spins are flipped in their orientation which can be compared to reversing the direction of their precession. The faster

precessing spins are now behind the slower ones. However this means, that the spins behind now have a slightly higher Lamor frequency and will catch up. Thus, after another TE/2, that is at the time the signal is read out, the spins are again phase coherent. However, the 180° pulse can only compensate for the dephasing caused by the static field inhomogenities of B_0, but cannot revert the effects caused by microscopic spin-spin interaction. The signal measured with SE is characterized by the intrinsic relaxation time constant T_2.
Images acquired with spin echo sequences have very good image quality, but due to their relatively long scanning time they are highly sensitive to motion [43].

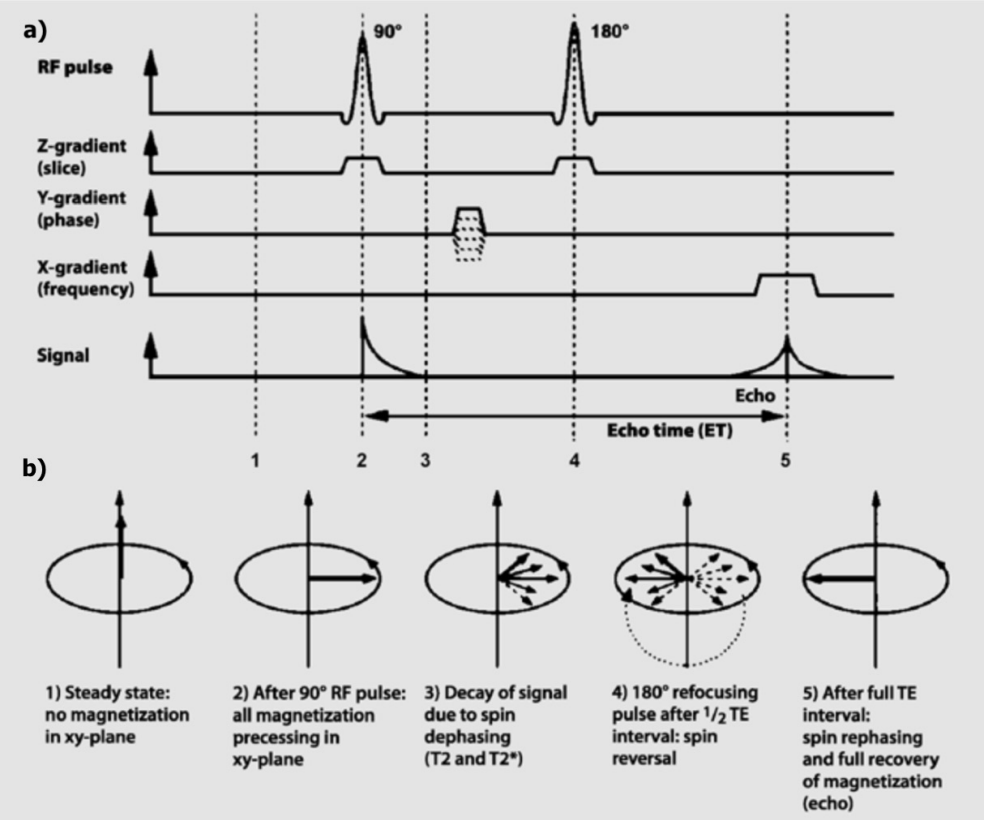

Figure 2.1: (a) Pulse timing diagram of a spin echo sequence. The time points **1-5** in the diagram correspond to the time points illustrated in (b). At time point 2, a 90° RF-pulse is applied simultaneously to the slice-selection gradient. Following, the signal begins to decay due to spin dephasing. At time point 4, a 180° refocusing pulse is applied to reverse the spins which leads to the rephasing of spins and an echo at time point 5. Note, that the phase encoding is done between time point 3 and 4 and also, that the 180° refocusing pulse is applied at the center between timepoint 2 and 5. **(b)** Illustration of echo generation in SE. Illustrations taken from [43].

Gradient Echo Sequences

Gradient echo (GRE) sequences use, as the name suggests, the magnetic field gradients to create an echo. This is done by applying a negative frequency-encoding gradient to dephase the spins. Subsequently, the gradient is reversed and the spins rephase to create an echo (see Figure 2.2). Since there is no 180° RF pulse, the repetition time TR can be kept short. This reduces the overall scan time drastically, which is a major advantage of GRE compared to SE sequences. Another effect is, that the spins dephase faster in a GRE sequence since the static magnetic field inhomogenities are not compensated by a 180° RF pulse and contribute to the signal decay. The signal in GRE imaging decays exponentially with the effective transverse relaxation time constant T_2^*

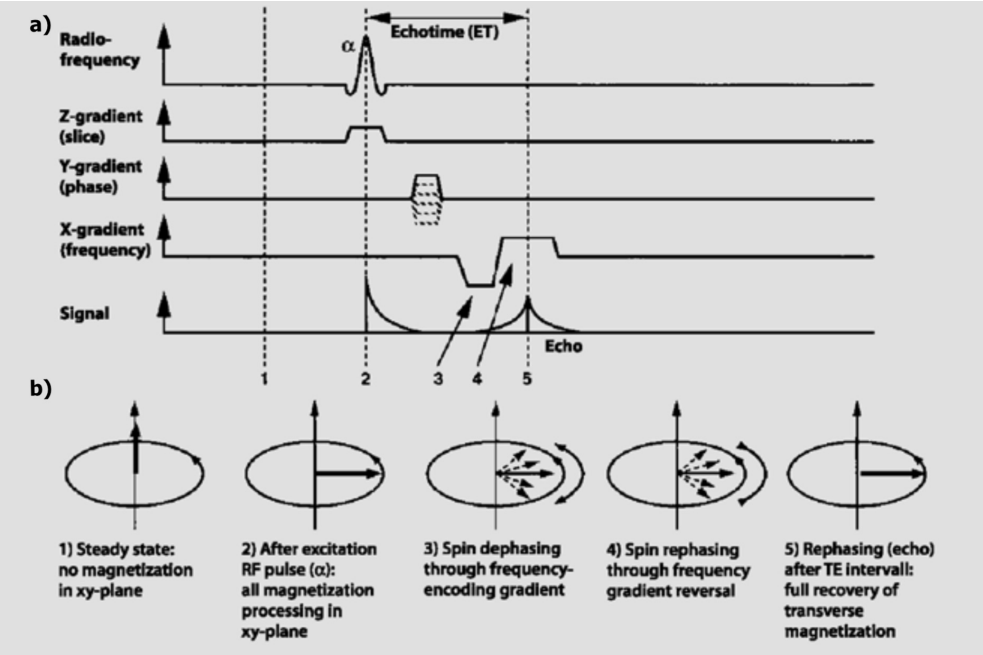

Figure 2.2: (a) Pulse timing diagram of a gradient echo sequence. The time points **1-5** in the diagram correspond to the time points illustrated in (b). At time point 2, a RF pulse with a nominal flip angle of α is applied simultaneously to the slice selection gradient. At time point 3, a negative frequency-encoding gradient is applied to dephase the spins. The gradient is then reversed at time point 4 to rephase the spins, leading to an echo at time point 5. Note, that the phase encoding is done between time point 2 and 3. **(b)** Illustration of echo generation in GRE. Note, that for simplicity, the flip angle α in 2) was chosen to be 90°, but can be chosen arbitrarily. Illustrations taken from [43].

2.1.3 Quantification of T1, T2/T2* and PD

In the previous sections, only qualitative image acquisition was introduced to obtain images weighted with the parameters T_1, T_2, T_2^*, and PD. For quantitative imaging, models are necessary to relate the signal characteristics to the absolute values of these parameters.
In the case of fast gradient echo imaging, the signal is given by the Ernst equation [8]:

$$S = A \cdot sin(\alpha)\frac{1 - e^{(-TR/T_1)}}{1 - cos(\alpha)e^{(-TR/T_1)}} \cdot e^{-TE/T_2^*} \tag{2.9}$$

where A is the initial signal amplitude, which is proportional to PD, α is the flip angle, TR is the repetition time, and TE is known as the echo time. The measurement of T_1 and PD in this work was based on the dependence of the steady-state signal in GRE images on TR and flip angle, which is referred to as the "variable flip angle technique" [22].
Equation 2.9 can be simplified for short TR (i.e. $TR/T_1 \ll 1$), and short TE (i.e. $TE/T_2^* \ll 1$) by approximating the exponential term with $e^{-TR/T1} \approx (1 - TR/T1)$ and the other exponential term with $e^{-TE/T_2^*} \approx 1$. This simplifies the equation in order to facilitate evaluation:

$$S \cong A \cdot sin(\alpha)\frac{TR/T_1}{1 - cos(\alpha)(1 - TR/T_1)}. \tag{2.10}$$

By applying the tangent half-angle substitution $t = tan(\alpha/2)$, leading to $sin(\alpha) = \frac{2t}{1+t^2}$ and $cos(\alpha) = \frac{1-t^2}{1+t^2}$, the equation can be further simplifyied by getting a rational term

$$S \cong A \cdot \frac{2t \cdot TR/T_1}{2t^2 + (1 - t^2) \cdot TR/T_1} \tag{2.11}$$

Now, T_1 and A can be calculated from signals S_1 and S_2 with different flip angles α_1 and α_2.
With $t_1 = tan(\alpha_1/2)$ and $t_2 = tan(\alpha_2/2)$, we get [12]

$$T_1 = TR \cdot \frac{(S_1/t_1 - S_2/t_2) + (S_2t_2 - S_1t_1)}{2(S_2t_2 - S_1t_1)} \tag{2.12}$$

and

$$A = \frac{S_1S_2(t_2/t_1 - t_1/t_2)}{2(S_2t_2 - S_1t_1)} \tag{2.13}$$

Quantitative T_2^* maps are estimated with an exponential fitting approach, commonly using weighted images acquired at different echo times. However, it has been

shown, that motion artifacts can be drastically reduced when the exponential fitting is done over echoes of multiple contrasts [46].
Assuming a monoexponential decay, the signal is described by:

$$S_{PD}(t) = S_{PD}(0) \cdot e^{-t/T_2^*} \tag{2.14}$$

$S_{PD}(t)$ refers to the signal of a PD weighted sequence. Now T_2^* is estimated by a log-linear fit, which is equivalent to minimizing the error ϵ:

$$\epsilon = \sum_{n=1}^{n_{max}} [ln(S_{PD}(TE(n))) + TE(n)/T_2^* - ln(S_{PD}(0))]^2 \tag{2.15}$$

where both $S_{PD}(0)$ and T_2^* are estimated. $TE(n)$ refers to time of the n^{th} echo, assuming equidistant echo times.
Analogously, T_2 maps can be estimated with the exponential fitting approach. While T_2^* are estimated from images acquired with GRE sequences, the estimation of T_2 requires data from SE sequences.

2.1.4 Coregistration

Image coregistration is the process of geometrically aligning two or more images, such that corresponding voxels in the different images represent the same region within an extended object. This is an absolute prerequisite, in order to do further quantitative post-processing, if several different contrasts are needed to reconstruct the image. Coregistration can be generally split into inter-subject coregistration between different individuals and intra- or within-subject coregistration of different images acquired from a single individual. Inter-subject coregistration is, for instance, necessary to compare the quantitative maps of individuals with each other in a group, or similarly to compare the maps of a patient with a healthy reference group. Intra-subject coregistration is useful to correct for motion, and for differences in sequence measurements [15]. Also, as described previously, intra-subject coregistration is important for the quality of the quantitative maps, which rely on recordings of multiple sequences such as in Weiskopf et al. [46].

Transformation and Cost functions

The goal of coregistration is to find a transformation to coregister the voxels in a map to the corresponding voxels in the reference map, which stays static. For inter-subject coregistration, non-linear coregistration is more appropriate due to variation in anatomical structures between different subjects. In the case of within-subject coregistration, a rigid transform is sufficient, which is essentially a combination of three rotations along each axis and three translations, since the skull of an individual is rigid and the brain moves little within the skull [15]. Thus, the problem

of coregistration can be reduced in this case to find appropriate parameters of the transformation matrix M. In order to evaluate how well the obtained transformation parameters align the images, a metric is required to measure the difference between the images. This metric is called the cost function. There are multiple ways to define cost functions; the most common ones are described briefly here.

Least squares

The probably most familiar way to measure the similarity of two images is to use the least-squares cost function, which can be defined as

$$C = \sum_{v=1}^{n} (A_v - B_v)^2 \tag{2.16}$$

where A_v and B_v refer to the v^{th} voxel of the respective image. However, this might not be very suitable in many cases, especially if both images have different intensity distributions, which is for intance the case between quantitative T_1 and PD maps.

Cross correlation

Another way to measure the similarity of two images is using the normalized cross correlation. This is defined as

$$C = \frac{\sum_{v=1}^{n} (A_v B_v)}{\sqrt{\sum_{v=1}^{n} A_v^2} \sqrt{\sum_{v=1}^{n} B_v^2}} \tag{2.17}$$

It can easily be seen, that the cross correlation equals 1, if A and B are identical and equals -1, if $A = -B$. The cross correlation is 0, if A and B are orthogonal.

Mutual Information

The mutual information cost function is based on the concept of entropy H of a random variable X, which is defined as

$$H = \sum_{i=1}^{N} p_i \cdot log(\frac{1}{p_i}) = -\sum_{i=1}^{N} p_i \cdot log(p_i) \tag{2.18}$$

where p_i is the probability of X to have the value x_i. If X is continous, then N refers to the number of grouped bins. For multiple images, entropy can be extended by analysing the so-called joint histogram, which shows the distribution of the frequencies of all possible combinations across all intensities of every voxel in the images. The joint entropy can then be computed as

$$H(A, B) = \sum_{i} \sum_{j} p_{i,j} \cdot log(\frac{1}{p_{i,j}}) \tag{2.19}$$

where $p_{i,j}$ is defined as $p_{i,j} = p(A = A_i \text{ and } B = B_j)$. Mutual information is then defined as as the difference between the sum of the entropies of each image and their joint entropy:

$$MI = H(A) + H(B) - H(A, B) \tag{2.20}$$

Since entropies are non-negtive, MI is maximal if $H(A, B)$ is minimal. This is the case, if B is most predictable from A. Therefore, mutual information can be used to measure the similarity between two images [30]. Studholme et al. showed in their paper, that a modified version, which they called normalized mutual information, defined as

$$MI = \frac{H(A) + H(B)}{H(A, B)} \tag{2.21}$$

provided significantly better behaviour [37].

2.1.5 Segmentation

Segmentation of brain images usually refers to the classification of brain tissue into gray matter, white matter and non-brain tissue. Segmentation methods can be broadly classified into two categories, either based on a tissue classification approach or by registration with a template. In the tissue classification approach, voxels are classified according to their intensity values. In order to do so, the intensity distribution of each tissue class needs to be identified, often by choosing voxels to represent each class. The other approach requires the registration of a template brain to the brain volume. This allows predefined regions in the template brain to be overlayed on the brain volume to identify different structures automatically [2].

2.2 Medical Magnetic Resonance Imaging

2.2.1 Conventional MRI

In magnetic resonance imaging there are two major subgroups, which are called functional MRI and structural MRI. As the name suggests, functional MRI focuses on the physiology of the human body with the aim to provide dynamic information, such as the blood flow through the brain.
In structural MRI, on the other hand, the anatomy of the human body is examined. Here the focus lies on providing static information, such as the volume or the shape of anatomical or pathological structures in the human brain [38]. By studying the images generated by MRI, different types of tissues, as well as abnormalities, such as lesions, oedemas, or tumours can be differentiated. This is possible since the difference in the chemical composition of different tissue types also leads to different magnetic properties of each tissue. Therefore, regions of different magnetic properties result in different signal intensities of the MR signal. Depending on the applied

pulse sequence different tissue types can appear very different. T_1-weighted, T_2-weighted, T_2^*-weighted, and proton density weighted sequences are among the most frequently used contrasts. For instance, in conventional T_1-weighted (T_1w) MRI, fat appears bright, while water appears dark. Note that the term "weighted" indicates that, although the specified parameter has the strongest effect on the contrast, the final contrast is also influenced by a combination of other physical parameters.

Various MRI protocol routines, consisting of a combination of different conventional MRI sequences, have already been broadly integrated into everyday clinical practice and are used for diagnosing a range of different medical conditions, ranging from a suspected stroke, brain tumours, epilepsy to neurodegenerative diseases, to name only a few. However, it is beyond the scope of this work to examine the whole spectrum of applications of conventional MRI. In the following, a few interesting examples are presented. A classical example is the detection of brain tumors in clinical MRI. Since brain tumors can be clearly delineated from surrounding tissue and due to the high resolution of MRI, MRI has become the method of choice, not only for the diagnosis of brain cancer, but also for treatment planning as well as for post-therapeutic brain evaluation. By injecting a contrast agent, such as Gadolinium chelats intravenously, the contrast between tumor and surrounding tissue is further enhanced [41].
T_2-weighted imaging is, for instance, used for detecting oedemas or distinguishing cysts from solid tumors and T_2^*-weighted imaging is suitable for illustrating methemoglobin, deoxyhemoglobin, or hemosiderin, due to its sensitivity to magnetic field inhomogeneities caused by susceptibility differences in different tissues. This means, that regions with higher concentration of the above named substances lead to a faster dephasing, and therefore, to a signal loss. Those regions appear dark in the image, as can be seen in the Figure 2.3.
Thus, T_2^*-weighted imaging is often often applied to detect pathologic conditions related to lesions and bleedings, including cerebral hemorrhage, tumour bleeding, or thrombosed aneurysm [6]. Furthermore, MRI has successfully been used in research to measure morphometric changes, such as the change of volume of the brain in ageing [10] or with learning [51].

2.2.2 Quantitative MRI

It is important to note here, that conventional MRI as described in Chapter 2.1.1 can only be seen as qualitative imaging. This means, that absolute signal intensities obtained at one site could not be reproduced at another site, due to differences in hardware and pulse sequences [9]. From a clinical view, diagnosis based on conventional MRI has to rely on the visual inspection and interpretation of the physician. It is important to note that a pathology can only be distinguished from

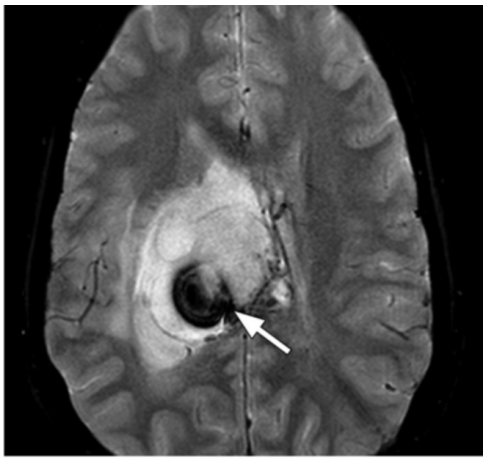

Figure 2.3: Axial T2*-weighted fast GRE MR image of a tumoral hemorrhage in a 17-year-old male adolescent with thalamic glioma. The arrow indicates the area of hemorrhage. Taken with courtesy of [6].

surrounding healthy tissue, if the pathology is also accompanied by structural or functional changes, which can be made visible in structural and functional MRI. However, if the pathology is systemic, it is impossible to detect with conventional MRI.
Quantitative MRI, however, uses the signal intensity to estimate the absolute values of a single physical or chemical parameter such as the T_2 transverse relaxation time or the proton density, in each voxel of the brain. From a research perspective, this is also advantageous since the quantitative estimation of physical or physiological parameters are site-independent. Therefore, not being limited to data from a single site increases the potential size of the patient cohort dramatically, which consequently increases statistical power.
As mentioned above, conventional MRI relies highly on contrast differences to differentiate between healthy and diseased tissue, but is mostly insensitive to subtle global changes of tissue compositions. In quantitative MRI, in contrast, a comparison between the value maps of a single subject and normative values acquired from a healthy reference group is feasible, for instance, to monitor subtle changes of the brain caused by disease [29]. Finally, there have been approaches to use these quantitative values as biomarkers for malignancy [48].

In the following, an interesting example is presented. Quantitative mapping of T_1 values in glioblastoma patients, as was investigated by Müller et al., detected cloudy-enhancing tumour compartments, which were not visible in conventional MRI [23]. By measuring the change of volume of these compartments during radio-chemotherapy, they were able to predict the length of the progression-free survival of the patients. These compartments were visible in the area surrounding the solid-tumour and it is suggested that this may represent tumour infiltration.

3 Methods

3.1 Description of dataset

The dataset used in this work was acquired in five healthy subjects (2 males and 3 females, aged 23-49) and eight post-operative glioma patients (5 males and 3 females, aged 33-67). who were scanned on a Philips 3T Ingenia Elition using a 32-channel head-coil. For quantitative mapping of T_1, PD and T_2^*, two 3D multi-echo gradient-echo sequences were acquired at TR=18ms and TE1/ΔTE = 2.4 ms/2.4 ms with two different flip angles $\alpha_1 = 4^\circ$ and $\alpha_2 = 25^\circ$. Compressed SENSE (with acceleration factor CS = 6) was also applied to reduce the scan time. Compressed sensing is a signal processing method that allows to acquire and reconstruct sparse signals, which, in the case of MRI, can shorten the scan time considerably. In each case, six echo images, each consisting of 176 slices, were acquired with a field of view (FOV) of 240 mm $\times$ 240 mm $\times$ 176 mm and a voxel size of 1 mm $\times$ 1 mm $\times$ 1 mm. Another 3D multi-echo Gradient-Spin-Echo (GraSE) sequence consisting of 8 echoes was acquired with a flip angle of $\alpha = 90^\circ$, and TE1/ΔTE/TR = 16 ms/16 ms/251 ms, which was used for T_2 mapping. The FOV was 224 mm $\times$ 192 mm $\times$ 115.5 mm with a voxel size of 2 mm $\times$ 2 mm $\times$ 3.3 mm. For mapping the actual flip angle, a sequence with a voxel size of 3.5 mm $\times$ 3.5 mm $\times$ 5 mm, a nominal flip angle of $\alpha = 60^\circ$, and TE1/TR1/TR2 = 2.3 ms/30 ms/150 ms was acquired and the actual flip angle imaging (AFI) method [50] was applied. The total scanning time including all three sequences and B1 mapping was 8:45 min.

Four other sequences acquired in the usual dignostic protocol for glioma patients, were used for the oedema segmentation. Two 3D T_1w gradient-echo sequences, each consisting of 267 slices, were acquired at TE/TR = 3.998 ms/9 ms, $\alpha = 8^\circ$, and compressed SENSE (with acceleration factor CS = 7.5), one before and the other after application of contrast agent, with a FOV of 252 mm $\times$ 252 mm $\times$ 200 mm and a voxel size of 0.75 mm $\times$ 0.75 mm $\times$ 0.75 mm. A T_2w sequence with fluid suppression (FLAIR), consisting of 281 slices, was acquired at TE/TI/TR = 326.29 ms/1650 ms/4800 ms, $\alpha = 90^\circ$, and compressed SENSE (with acceleration factor CS = 10), with a FOV of 250 mm $\times$ 250 mm $\times$ 200 mm and a voxel size of 0.71 mm $\times$ 0.71 mm $\times$ 0.71 mm. Finally, a 2D spin-echo, consisting of 38 slices, was acquired at TR/TE = 3088 ms/79.82 ms, $\alpha = 90^\circ$, and compressed SENSE (with acceleration factor CS = 1.5), with a FOV of 230 mm $\times$ 230 mm $\times$ 167 mm and a voxel size of 0.36 mm $\times$ 0.36 mm $\times$ 4.4 mm.

3.2 Structure of pipeline

In order to evaluate multiple different quantitative datasets sequentially and automatically, a pipeline for data processing and analysis was developed. This means, that all datasets can be evaluated sequentially without the need of user intervention. This makes the analysis process much less time consuming and less prone to errors from changes in manual inputs.
The pipeline was implemented in Matlab and made use of the software packages hMRI toolbox [39] and the brain extraction tool (BET) [36] of the FMRIB Software Library [49]. Also, MRIcron [34], a cross-plattform Neuroimaging Informatics Technology Initiative (NIfTI) format image viewer, was used for visual inspections.
During each scanning procedure, multiple imaging sequences were acquired. The resulting images were exported from the MRI scanner in the DICOM (Digital Imaging and Communications in Medicine) file format, an international standard to transmit, store, process, and display medical imaging information [7]. However, it is quite cumbersome to work with images in DICOM format in post-processing, particularly because DICOM is a 2D image file format and 3D volumes are described as a series of DICOM 2D images. This means that up to several thousand of separate files are stored after each scanning procedure, which has become unhandy. For post-processing the NIfTI file format [25] is more preferable, particularly because it can be used to save images as 3D volume. This is why the NIfTI format has been adopted to be the default format in many widespread software packages, such as in the statistical parametric mapping (SPM) framework or in the FMRIB software library (FSL) framework [19]. In this pipeline, the output datatype was thus chosen to be NIfTI, while the input datatype was DICOM. The overall structure of the pipeline can be seen in Figure 3.1a.

In order to be processed correctly by the pipeline implemented in this work, all images belonging to one subject need to be stored in DICOM format in a folder called "DICOM". This folder must be located in an arbitrarily named folder with the name for this dataset, e.g. "Dataset 1". All dataset-folders need to be in the same arbitrarily named parent folder, e.g. "Data". This folder structure is also illustrated in Figure 3.1b. An illustration of the processing procedure implemented in the pipeline can be found in Figure 3.2 and is described in the following.
In the first step, the header of each DICOM file in the subfolder 'DICOM' is read in sequentially. The protocol name parameter in the DICOM header indicates, which sequence the DICOM file belongs to. According to the protocol name, the DICOM file is moved to the respective, eponymous subfolder. Subfolders for the protocol names "B1 map Yarnykh", "T1w fa25", "PDw", and "T2 3D GRASE" are created in advance, because they are required for further processing of quantitative parameter maps (qMaps). For every additional sequence, a new subfolder is created to store the respective DICOM files.
A final subfolder 'Analysis' is also created, where the final qMaps of the brain will be

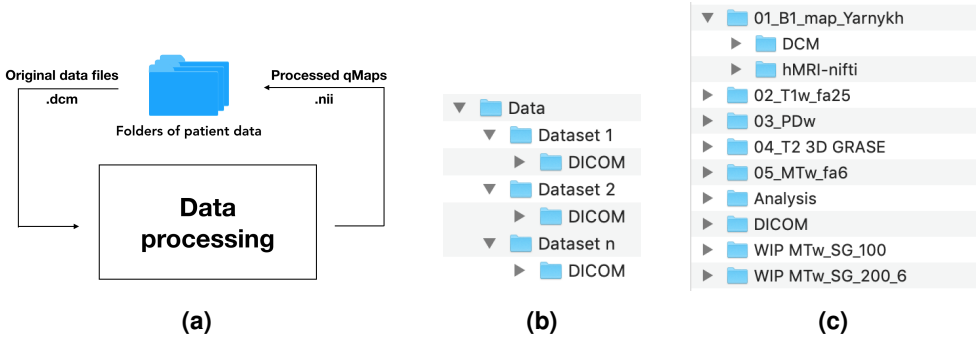

Figure 3.1: (a) Macrostructure of data processing pipeline. The extensions .dcm and .nii refer to the file formats DICOM and NIfTI respectively. **(b)** Folder structure of input datasets. A simple folder structure is a prerequisite for the pipeline to work properly. Here, the overall parent folder is called "Data" and the datasets "Dataset 1", "Dataset 2"... each have a subfolder "DICOM". **(c)** Exemplary final folder structure. Note that subfolders starting with 'WIP' are additional sequences recorded from the same subject, which are also part of the dataset, but not needed for further analysis.

stored after processing. The final folder structure can be found in Figure 3.1c.
The next step is the conversion of all DICOM files of one sequence to one 3D NIfTI file. This is performed for all sequences for each dataset. If the dataset contains other sequences, which are not required for quantitative mapping, the DICOM files of these sequences are also converted to NIfTIs, but are not used for further processing.
After this sorting step, the NIfTI files of the sequences 'B1 map Yarnykh', 'T1w fa25', and 'PDw' are used to generate quantiative PD, R_1 and R_2^* maps, using the hMRI toolbox, with R_1 and R_2^* being the reciprocal values of $T_1 = 1/R_1$ and $T_2^* = 1/R_2^*$. The NIfTI files of the sequence 'T2 3D GRASE' are used to estimate a T_2 map. The hMRI toolbox as well as the method to estimate the T_2 map is elaborated later in the subsections 3.2.2 and 3.2.3 respectively. As a final step, brain tissue is segmented from non-brain tissue, such as the eyeballs, skin, fat, muscle, etc., which are also recorded in a MR image. For this, the brain extraction tool of the FSL toolbox [49][36] is used. This results in qMaps restricted to the brain tissue volume. These qMaps are further segmented into gray and white matter tissue maps using the "Segment" tool of the hMRI toolbox to evaluate the quantitative values inside the volume of interest (VOI). Subsequently to the creation of the quantitative maps, a segmentation of the oedema surroung the glioma is performed if the data is from a glioma patient, using BraTS (Brain Tumor Segmentation) orchestra, an ensemble code developed by Kofler et al., based on docker images used in the BraTS Challenge 2018 [16]. In particular, the docker image of an implementation presented in [24] is used.
The segmented oedema is then used as a mask to analyze the particular region of interest in the quantitative maps.

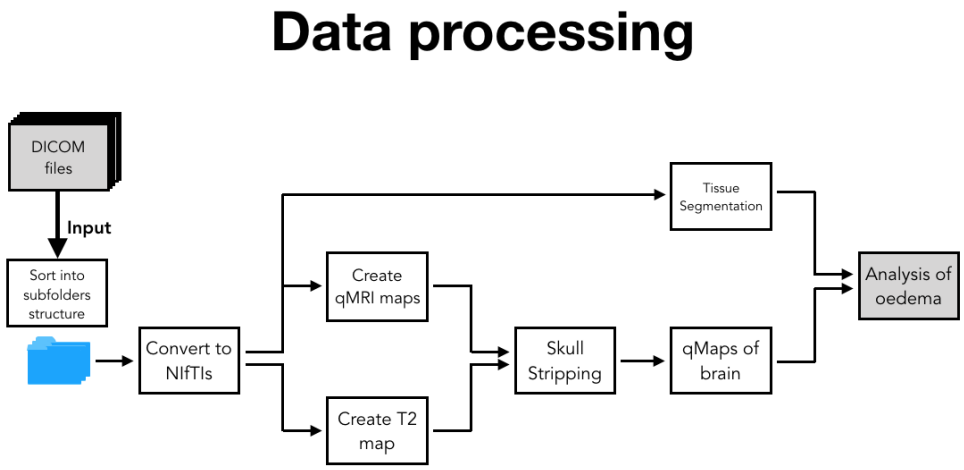

Figure 3.2: Detailed illustration of the data processing. The input of the pipeline are DICOM files belonging to one dataset. These files are first sorted into subfolders, according to the protocol name parameter in their header file. DICOMs inside the same subfolder belong to the same MRI sequence. Next, the DICOM files inside each folder are converted into a 3D NIfTI volume. Depending on the type of sequence, these NIfTI volumes are either used for quantitative mapping or tissue segmentation into oedema, gray matter, and white matter. Subsequently, the quantitative maps are skull stripped. The segmented oedema and the skull stripped qMaps are used together to analyse the oedema.

3.2.1 FSL Toolbox and Brain Extraction Tool

The FMRIB software library was created by the analysis group of the Wellcome centre of integrative neuroimaging in Oxford [49]. It is a comprehensive library of analysis tools for FMRI, MRI and DTI brain imaging data, which runs both on macOS and Linux. The brain extraction tool (BET) [36], which is used as part of this work, can be run both from command-line or with a Graphical User Interface (GUI). In this work, BET is run from command-line, called from inside a Matlab script. BET is an fully automated method, which segments MR images of the human head into brain and non-brain tissue, which is also known as skull-stripping. It is based on a deformable model that evolves to fit the brain's surface.
In this work, BET was used to improve the results of the oedema segmentation and the segmentation into different tissue types used in the validation process.
BET is applied to the estimated quantitative PD Map, which worked best for skull stripping, and the extracted brain mask was then applied to all qMaps. The quality of skull stripping was checked visually by overlaying the extracted brain on the original MRI with MRIcron.

3.2.2 SPM and hMRI Toolbox

The hMRI toolbox is a framework for multi-parametric quantitative MRI written in Matlab, developed by Tabelow et al. [39] for applications in neuroscience and clinical research. It is embedded into the SPM framework and can be used together with the established tools of the SPM framework. All of the tools can be run from a GUI, but there is also an option to save batches and scripts for setting up an automatic pipeline. The toolbox is organised into five main modules, from which the modules "Configure Toolbox", "DICOM import" and "Create hMRI maps" are used in this work. In the module "Configure Toolbox", some acquisition and processing parameters are customized. As the name suggests, the module "DICOM import" imports DICOM files and converts them into the NIfTI format. This module must be run for every subject and every sequence separately. In this work, a default batch was created, which converts all DICOM images inside each subfolder called 'DCM', such that the image format conversion is automated. Lastly, "Create hMRI maps" is used for the calculation of quantitative PD, R_1, and R_2^* maps. The creation of these qMaps is based on the MPM multi-echo protocol introduced by Weiskopf et al. in [44] and [47]. The maps created in the hMRI-toolbox are additionally corrected for the bias introduced by B1 transmit field inhomogenities, if specific B1 transmit field measurements were acquired. In this work, the Actual Flip Angle Imaging (AFI) method [50] was applied for B1 mapping.
Furthermore, the tools "Coregister and Reslice" and "Segment" of the SPM framework are used as well. The "Coregister and Reslice" tool coregisters and reslices a source image to a given reference image. This is important, as has been elabo-

rated in the fundamentals section, to ensure that voxels at the same position of two different images refer to the same position in the brain. Also, since the sequences are acquired at different FOV and resolutions, reslicing is necessary to make voxel-based operations, such as masking images, applicable on every acquired image. With the help of the "Segment" tool, a given MR image can be segmented into probability maps of white matter tissue, gray matter tissue, cerebrospinal fluid, air, and skull. This tool is used in the validation process and in the analysis of glioma patients. The results are improved if a skull stripped MR volume is provided.

3.2.3 T2 Map Generation and Evaluation

The estimation of the T_2 map by mono-exponential fitting was implemented in Matlab according to a method proposed by Pei et al. [28]. This method is based on Auto Regression on Linear Operation (ARLO) and was chosen over Non-linear least squares based Levenberg-Marquard and Log-Linear, since it proved to be both fast and more accurate [28].
Assuming an ideal signal of a SE sequence, the amplitude of the signal $m(TE)$ can be expressed by a mono-exponential decay:

$$m(TE) = M_0 \cdot e^{-TE/T_2}, \tag{3.1}$$

where TE is the echo time and M_0 is the proton density scaled by multiple sequence and hardware parameters. By integrating $m(TE)$ over two consecutive echoes from the i^{th} echo time TE_i onwards, we get

$$s_i = \int_{TE_i}^{TE_{i+2}} m(t)dt = T_2 \cdot [m(TE_{i+2}) - m(TE_i)] \equiv T_2\delta_i, \tag{3.2}$$

where $\delta_i = [m(TE_{i+2}) - m(TE_i)]$, $i = 1, ..., N-2$, and N is the number of echoes.
Assuming echo-intervals of the same length of ΔTE, the integral can be approximated numerically to the 4^{th} order of accuracy with Simpson's rule [1]:

$$s_i \cong \frac{\Delta TE}{3} \cdot [m(TE_i) + 4m(TE_{i+1}) + m(TE_{i+2})]. \tag{3.3}$$

T_2 can then be found as the maximum-likelihood estimate by minimizing the following cost function $C(T_2)$:

$$min(C(T_2)) = \min_{T_2} \sum_{i=1}^{N-2} \left(m(TE_{i+2}) + \frac{\frac{4\Delta TE}{3}}{T_2 + \frac{\Delta TE}{3}} \cdot m(TE_{i+1}) - \frac{T_2 - \frac{\Delta TE}{3}}{T_2 + \frac{\Delta TE}{3}} \cdot m(TE_i) \right)^2, \tag{3.4}$$

which simplifies to

$$T_2 = \arg\min_{T_2} \frac{1}{\left(T_2 + \frac{\Delta TE}{3}\right)^2} \sum_{i=1}^{N-2} (s_i - T_2 \cdot \delta_i)^2, \tag{3.5}$$

with the definitions of s_i and δ_i from above. This minimizer can be analytically solved, such that T_2 can be explicitally expressed as

$$T_2 = \frac{\sum_{i=1}^{N-2}(s_i^2) + \frac{\Delta TE}{3} \cdot \sum_{i=1}^{N-2}(s_i\delta_i)}{\frac{\Delta TE}{3} \cdot \sum_{i=1}^{N-2}(s_i^2) + \sum_{i=1}^{N-2}(s_i\delta_i)}. \tag{3.6}$$

For a detailed derivation of the above minimizer, please refer to [28].

3.3 Validation

There are essentially three parts, which have been validated in this work. First of all, the pipeline needs to generate the same quantitative maps as the usage of the GUI with a manual map generation. For validation, five datasets of healthy subjects were used, which previously have been manually evaluated by an experienced user, using the graphic user interface (GUI) of the hMRI-toolbox, on a Linux (Ubuntu 16.04 LTS and with Matlab version 2017b).
The first part of the validation tackled the question, whether the same dataset exported directly from the MR scanner or retrospectly from the clinical Picture Archiving and Communication System (PACS) yields the same quantitative maps.
After initial tests, it was also noticed that different parts of the pipeline and parameters, such as the subversions of the SPM framework or a different scaling parameter used in the DICOM to NIfTI conversion have significant, partially strong, impact on the final quantitative maps.
Thus, the second part of the validation process consisted of systematical testing, which configuration of parameters led to the minimal relative difference per voxel between pipe-generated and manually generated qMaps. The parameters taken into consideration were the operation system (macOS versus Linux), the subversions of the SPM framework (version 6225 versus version 7487), the influence of two different scaling factors in the DICOM header used for the conversion to NIfTIs ("RescaleSlope" vs "MRScaleSlope"), and finally, the inclusion of additonal data in the processing process (inclusion of data from a magnetic transfer (MT) sequence versus no additional data). The scaling is needed to adjust the intensities from data acquired with different echo times and different flip angels, which is important for quantitative evaluation. The macOS version used for comparison was macOS Mojave 10.14.3.
For qualitative comparison, a map of relative differences per voxel was generated,

which was inspected visually. Additionally, the mean and standard deviation of these differences were calculated for quantitative evaluation. The configuration of parameters, which generated qMaps closest to the reference maps, was used in the third part of the validation and in the analysis of data from glioma patients, which is described in the following.
The third part of the validation consisted of the comparison of absolute measured parameter values of gray and white matter in the generated quantitative maps with literature values. The probability maps of gray and white matter were used with a binary threshold of 0.75 to create a mask of only white or gray matter tissue, respectively and to calculate the mean and standard deviation of the quantitative values of each qMap. The mean of these quantitative parameter values were then compared with literature values.

3.4 Analysis of Glioma Patients

Finally, after the different steps of the validation process ensured that the pipeline produced reliable qMaps, the last part of this work consisted of analysing the qMaps of glioma patients. There were two main questions of interest: First, the quantitative values of PD, R_1, R_2^*, and T_2 in the oedema surrounding the space of resection of the glioma. Second, the question whether quantitative values of these parameters were affected globally in the non-pathological gray and white matter in the glioma patients.

4 Results

4.1 Technical Procedure

The pipeline implemented in this works fully automatic on both, datasets exported directly from the scanner and datasets exported from the PACS, which vary slightly in their DICOM header. On average, the processing of each dataset from the original DICOM files to the quantitative maps took around 18 minutes, while the glioma segmentation on a 2,2 GHz Intel Core i7 CPU took approximately 45 minutes. If DICOM files of additional sequences were included in the dataset, the processing time increased. Further statistical analysis, including the reslicing of NIfTIs for masking, took no longer than a few minutes.
For the separate analysis of both hemispheres in glioma patients, the border between both hemispheres was chosen manually after visually inspecting the brain volume in MRIcron.
An illustration of the pipeline with input and output images after each step can be found in Figure 4.1. The cross section of a healthy subject and a glioma patient, as well as an exemplary segmentation of the brain into VOIs can be found in Figures 4.2 and 4.3, respectively.

4.2 Quality of Quantitative Evaluation

4.2.1 Data from Scanner vs. Data from PACS

Since a dataset can be either exported directly from the MR scanner after an examination or retrospectively from the PACS, this evaluation examined, whether the quantitative maps of the same dataset deviated from each other depending on the method of data export. Reassuringly, the results were identical. However, an adjustment in the processing pipeline was necessary to achieve the same result: Since the DICOM headers are changed in the archiving process of PACS, the scaling parameter necessary for appropriate scaling of the image intensities was stored under a different structure field compared to DICOM files exported directly from the scanner. Thus, it was necessary to figure out which scaling parameter to use for proper scaling, since otherwise it would result in considerable deviations in the resulting qMaps.
Parameter selection was implemented case-dependent in the script for DICOM to NIfTI conversion to circumvent this issue.

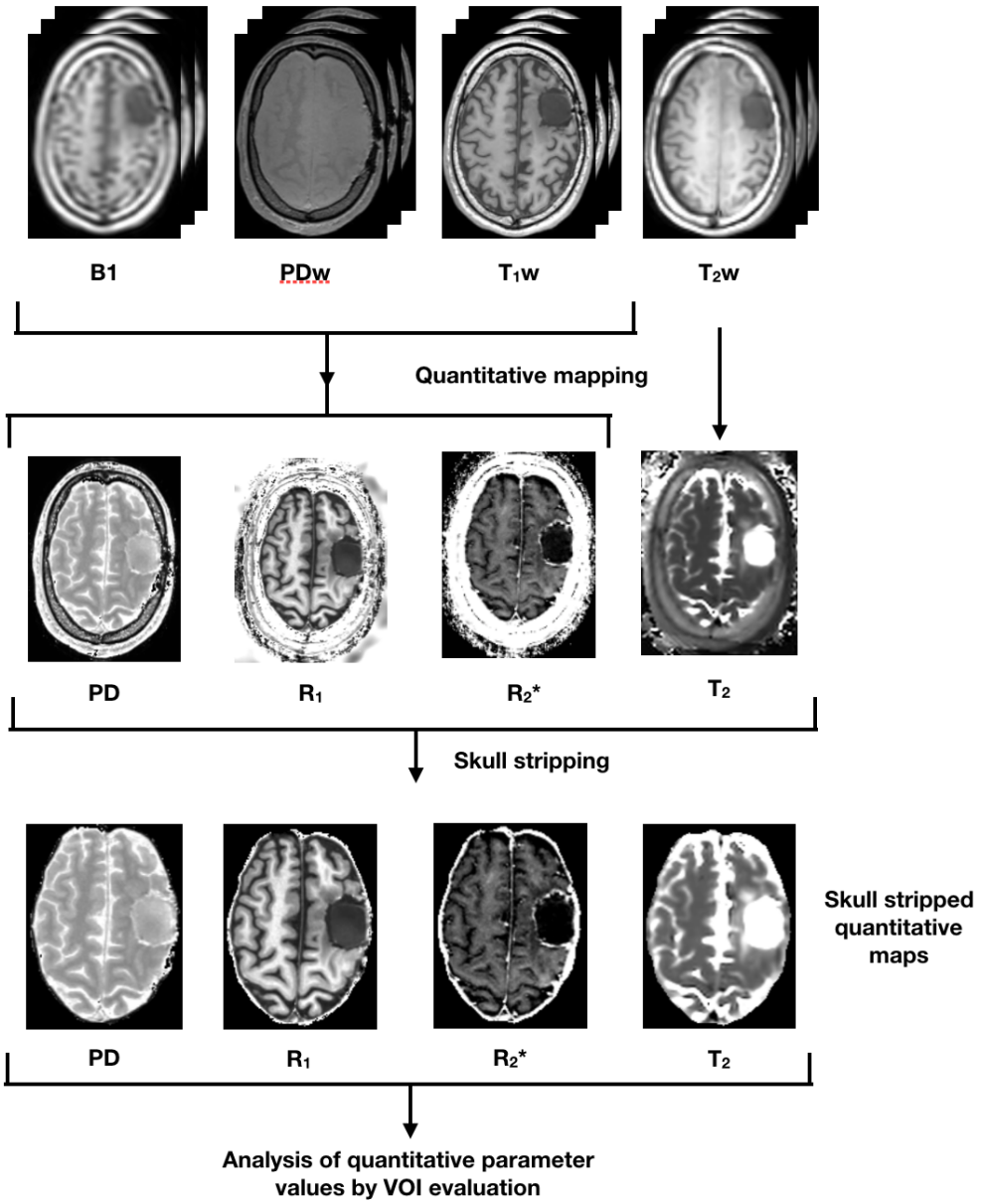

Figure 4.1: Illustration of the workflow within the pipeline with input and output images after each step. The top row illustrates the weighted input images for quantitative mapping. The middle and bottom rows show calculated parameter maps before and after skull stripping. Note, that multiple image volumes of the weighted sequences are used for quantitative mapping. Note also, that VOI stands for volume of interest.

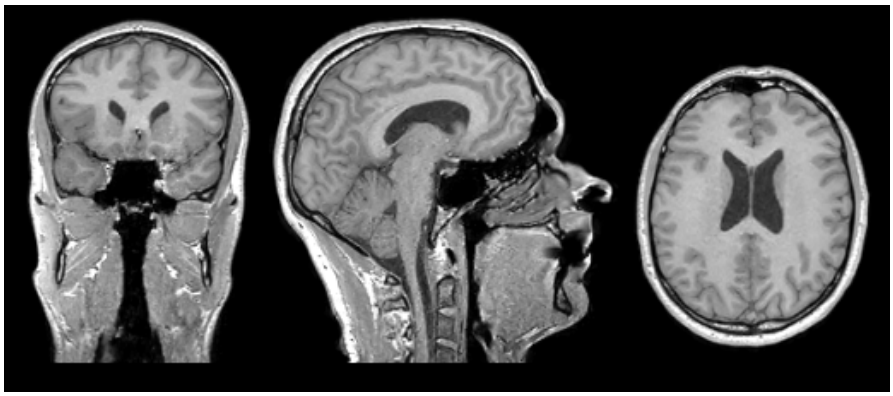

(a)

(b)

Figure 4.2: (a) Exemplary slices of a T_1w data set from a healthy volunteer in different orientations.**(b)** Segmented gray and white matter overlayed on the same slices of the T_1w data. Gray matter is depicted in red and white matter depicted in purple.

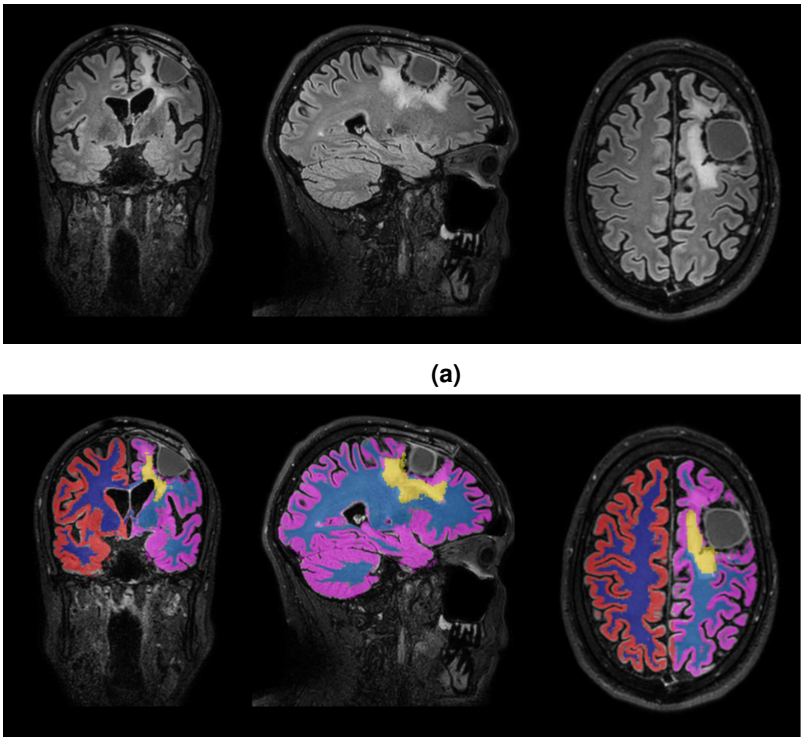

(a)

(b)

Figure 4.3: (a) Exemplary FLAIR images of a glioma patient in different orientations. **(b)** Segmented oedema (yellow) and gray and white matter of each hemisphere overlayed on FLAIR images of a glioma patient. In the unaffected hemisphere, gray matter is depicted in red and white matter is depicted in dark-blue. In the affected hemisphere gray matter is depicted in pink and white matter is depicted in light-blue.

4.2.2 Quantitative Evaluation with Different Parameter Configurations

Sixteen different configurations were evaluated to examine which configuration led to qMaps closest to the reference qMaps, which were taken as "ground-truth". The results of these evaluations can be found in Figure 4.4a. The configuration settings of each configuration number can be found in Table 4.4b. The reference qMaps were generated by an experienced user using the GUI of the hMRI toolbox.
For each subject and each qMap, the relative deviation was calculated as the relative difference per voxel between the calculated qMap and the reference qMap, averaged over the number of voxels inside the skull-stripped volume. These relative deviations were then averaged over all subjects to get more robust results. It can be seen that the relative deviations of the R_1 maps are below $1\,\%$ and remain nearly unaffected from the configration settings. Also, it can be noticed, that in every configuration without inclusion of an additional MT sequence for qMap estimation (i.e. every even numbered configuration), the relative deviation of the R_2^* is constantly very high at just below $12\,\%$, while in every configration with an additional MT sequece for qMap estimation (i.e. every odd numbered configuration), the relative deviation is close to zero. The relative deviation of the PD map varies between just below $1\,\%$ and around $12\,\%$, among which configurations including MT files had relative deviations between $1\,\%$ and $5\,\%$, while configurations without MT files had larger relative deviations ranging from $8\,\%$ to $12\,\%$. The change of the operation system accounted for up to $2\,\%$ relative deviation.
The configuration with the lowest deviations was configuration number 11 with mean relative deviations per voxel of $0.73\,\%$, $0.15\,\%$, and $0.18\,\%$ in the PD, the R_1, and R_2^* map, respectively. The relative deviations in configuration 3 were $0.97\,\%$, $0.046\,\%$, and $0.080\,\%$ in the PD, the R_1, and R_2^* map, respectively. Configuration 3 was used for further analysis, since its deviations were only marginally larger for the PD map and even smaller for the R_1 and R_2^* map and the macOS was much better accessible.

4.2.3 Validation of Values in Quantitative Maps

The quantitative maps of the five healthy subjects were also validated with regard to their quantitative values in comparison with values found in literature. In Figure 4.5, the minimum and maximum of the quantitative values found in literature are compared with the values estimated in this study. Additionally, the range of literature values is also highlighted in the Figures 4.6, 4.7, 4.8, and 4.9 of section 4.3.

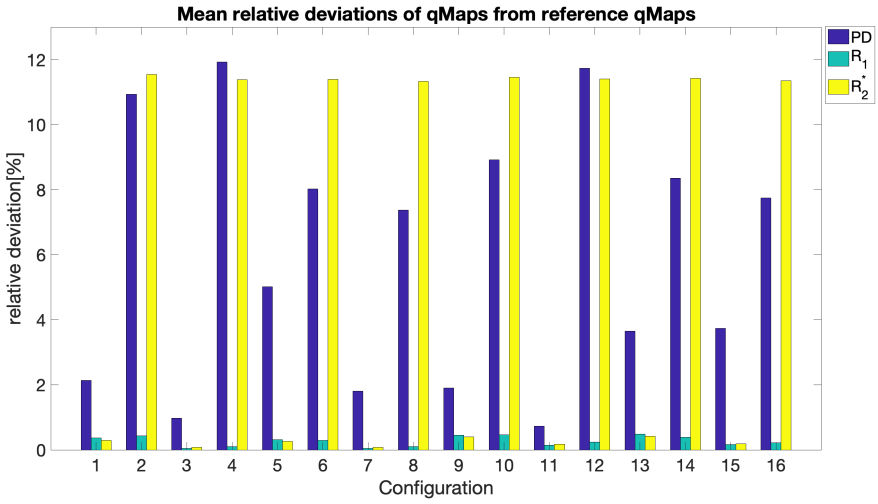

(a)

Configuration	OS	SPM version	Rescale factor	MT files
1	macOS	spm12 v6225	MRScaleSlope	Yes
2	macOS	spm12 v6225	MRScaleSlope	No
3	macOS	spm12 v6225	RescaleSlope	Yes
4	macOS	spm12 v6225	RescaleSlope	No
5	macOS	spm12 v7487	MRScaleSlope	Yes
6	macOS	spm12 v7487	MRScaleSlope	No
7	macOS	spm12 v7487	RescaleSlope	Yes
8	macOS	spm12 v7487	RescaleSlope	No
9	Linux	spm12 v6225	MRScaleSlope	Yes
10	Linux	spm12 v6225	MRScaleSlope	No
11	Linux	spm12 v6225	RescaleSlope	Yes
12	Linux	spm12 v6225	RescaleSlope	No
13	Linux	spm12 v7487	MRScaleSlope	Yes
14	Linux	spm12 v7487	MRScaleSlope	No
15	Linux	spm12 v7487	RescaleSlope	Yes
16	Linux	spm12 v7487	RescaleSlope	No

(b)

Figure 4.4: (a) Mean relative deviations of qMaps for different configurations from reference qMaps derived by manual evaluation by an experienced user. The mean deviation was calculated as VOI average across voxel-wise relative deviations between the calculated qMaps and the respective "ground-truth" reference qMaps and averaged over five healthy subjects. Please refer to the table in (b), to see the description of each configuration. **(b)** Configurations examined in the quantitative evaluation. The macOS version used was macOS Mojave 10.14.3, the Linux version used was Ubuntu 18.04.3 LTS, the reference qMaps were evaluated on a Linux with Ubuntu 16.04 LTS. The SPM version refers to the subversion of SPM, which was used in the pipeline. The rescale factor is a field in the DICOM header used for the DICOM to NIfTI conversion. The column "MT files" refers to whether an additional MT sequence was included in the qMap estimation.

Volume of interest	$\mathbf{PD}$ [%]	$\mathbf{R_1}$ [$\mathbf{s^{-1}}$]	$\mathbf{R_2^*}$ [$\mathbf{s^{-1}}$]	$\mathbf{T_2}$ [ms]
GM healthy	77.63 ± 0.64	0.666 ± 0.015	20.93 ± 0.70	-
GM literature values	[78, 84]	[0.625, 0.724]	[15.2, 18.5]	[64.8, 120]
WM healthy	68.65 ± 0.29	0.991 ± 0.014	24.52 ± 0.70	-
WM literature values	[68, 71]	[0.923, 1.204]	[19.5, 21.0]	[55.8, 76.2]

.

Figure 4.5: Quantitative parameter values (mean $\pm$ standard deviation ($\mu \pm \sigma$)) in gray matter (GM) and white matter (WM) over five healthy subjects compared with literature values found in [11], [14], [18], [31], [32], and [47]. For literature values, the range between minimal and maximal reported values is provided. The literature values are also highlighted in the Figures 4.6, 4.7, 4.8, and 4.9 of section 4.3. Note, that no T_2 data of healthy subjects was available.

4.3 Results of Quantitative Analysis

Finally, the pipeline was used to analyse the quantitative parameter values inside the brain of glioma patients. For this purpose, the PD, R_1, R_2^*, and T_2 values in five volumes of interest (VOI) were examined. The VOIs comprised the gray and white matter, each of the affected and the non-affected hemisphere as well as the segmented oedema. For each patient, the values were calculated by taking the mean over all voxels inside the VOI.
The results of this analysis (Figures 4.6, 4.7, 4.8, and 4.9) are shown together with the quantitative parameter values within grey matter and white matter of healthy subjects. In order to compare potential differences between both hemispheres, values belonging to the same patient in the same type of tissue were connected with a line in each plot. The mean and standard deviation over all glioma patients can be found in Table 4.5.

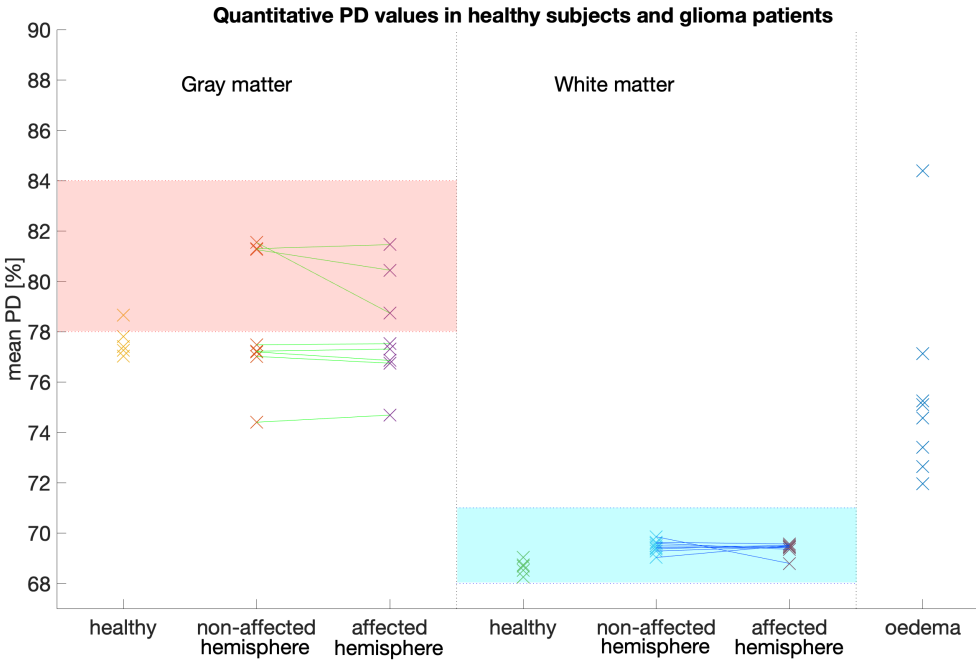

Figure 4.6: Comparing quantitative PD values in healthy subjects (# subjects: 5) and glioma patients (# patients: 8). Comparing 7 VOIs in three groups: Gray matter, white matter and oedema. Values belonging to the same patient and the same tissue type are connected with a line. "Healthy" refers to the VOI average over both hemispheres of a healthy subject and "non-affected hemisphere" refers to the hemisphere of a patient not affected by the glioma, while "affected hemisphere" refers to the hemisphere affected by the glioma. "Oedema" refers to the VOI inside the segmented oedema. Please refer to Table 4.10 for mean and standard deviation of the data. Literature values of gray and white matter are highlighted in a red and light-blue shade, respectively and are taken from [11] and [47].

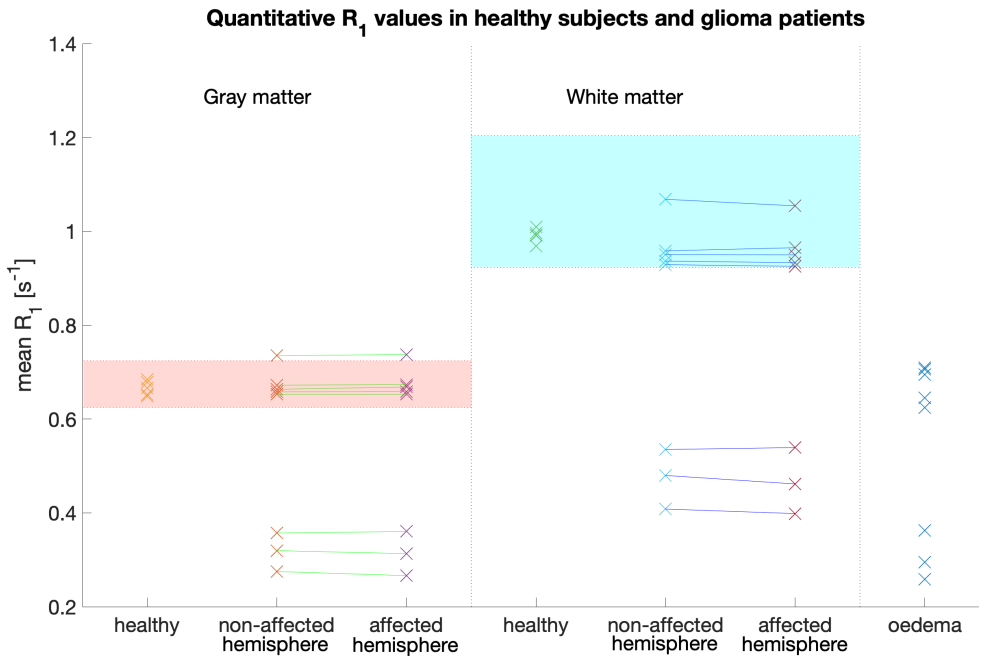

Figure 4.7: Comparing quantitative R_1 values in healthy subjects (# subjects: 5) and glioma patients (# patients: 8). Comparing 7 VOIs in three groups: Gray matter, white matter and oedema. Values belonging to the same patient are connected with a line. "Healthy" refers to the VOI average over both hemispheres of a healthy subject and "non-affected hemisphere" refers to the hemisphere of a patient not affected by the glioma, while "affected hemisphere" refers to the hemisphere affected by the glioma. "Oedema" refers to the VOI inside the segmented oedema. Please refer to Table 4.10 for mean and standard deviation of the data. Literature values of gray and white matter are highlighted in a red and light-blue shade, respectively and are taken from [31] and [32].

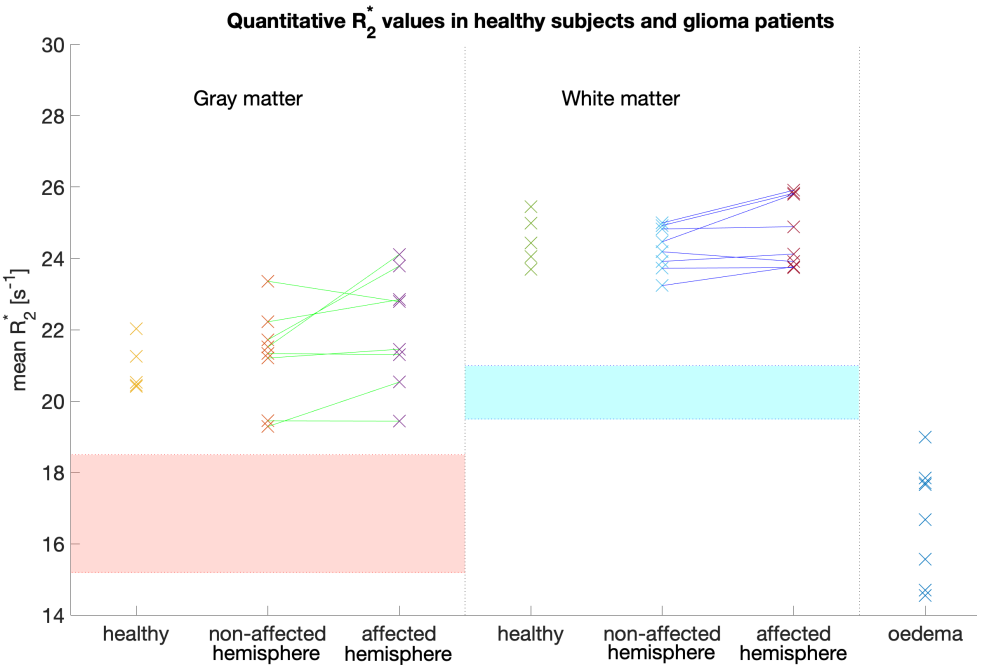

Figure 4.8: Comparing quantitative R_2^* values in healthy subjects (# subjects: 5) and glioma patients (# patients: 8). Comparing 7 VOIs in three groups: Gray matter, white matter and oedema. Values belonging to the same patient are connected with a line. "Healthy" refers to the VOI average over both hemispheres of a healthy subject and "non-affected hemisphere" refers to the hemisphere of a patient not affected by the glioma, while "affected hemisphere" refers to the hemisphere affected by the glioma. "Oedema" refers to the VOI inside the segmented oedema. Please refer to Table 4.10 for mean and standard deviation of the data. Literature values of gray and white matter are highlighted in a red and light-blue shade, respectively and are taken from [14] and [47].

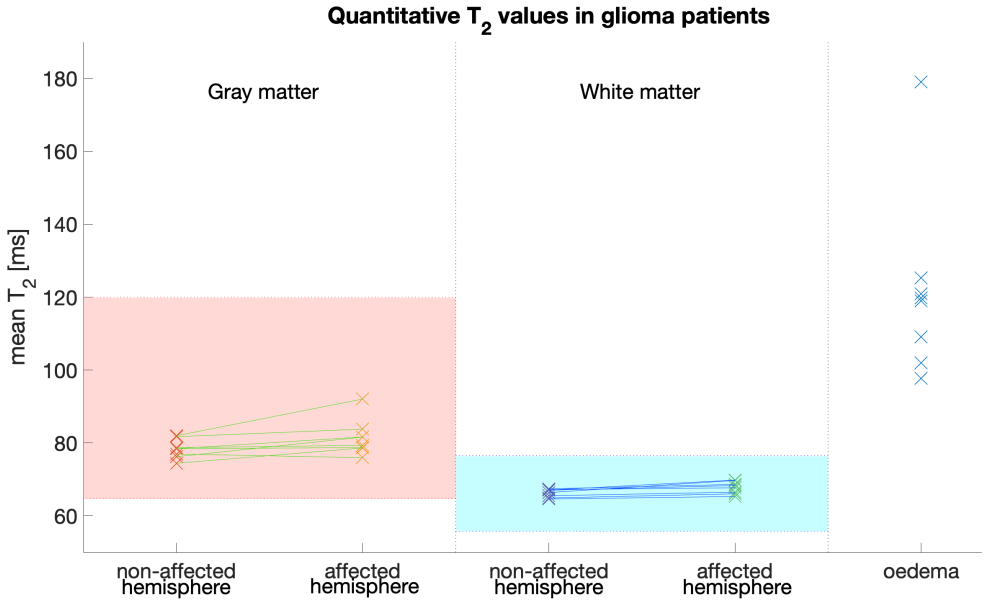

Figure 4.9: Comparing quantitative T_2 values in glioma patients (# patients: 8), since no T_2 data of healthy subjects was available. Comparing 5 VOIs in three groups: Gray matter, white matter and oedema. Values belonging to the same patient are connected with a line. "Non-affected hemisphere" refers to the hemisphere of a patient not affected by the glioma, while "affected hemisphere" refers to the hemisphere affected by the glioma. "Oedema" refers to the VOI inside the segmented oedema. Please refer to Table 4.10 for mean and standard deviation of the data. Literature values of gray and white matter are highlighted in a red and light-blue shade, respectively and are taken from [14] and [18].

Volume of interest	$\mathbf{PD}$ [%]	$\mathbf{R_1}$ [$\mathbf{s^{-1}}$]	$\mathbf{R_2^*}$ [$\mathbf{s^{-1}}$]	$\mathbf{T_2}$ [ms]
GM healthy	77.63 ± 0.64	0.666 ± 0.015	20.93 ± 0.70	-
GM non affected hemisphere	78.43 ± 2.62	0.542 ± 0.189	21.26 ± 1.35	78.36 ± 2.58
GM affected hemisphere	77.97 ± 2.17	0.541 ± 0.192	22.03 ± 1.62	81.47 ± 4.90
WM healthy	68.65 ± 0.29	0.991 ± 0.014	24.52 ± 0.70	-
WM non affected hemisphere	69.46 ± 0.25	0.783 ± 0.262	24.28 ± 0.63	66.27 ± 1.11
WM affected hemisphere	69.39 ± 0.25	0.778 ± 0.264	24.75 ± 0.98	67.75 ± 1.68
Oedema	75.56 ± 3.92	0.537 ± 0.196	16.71 ± 1.62	121.63 ± 25.16

Figure 4.10: Quantitative parameter values (mean $\pm$ standard deviation ($\mu \pm \sigma$)) in 7 VOIs over 5 healthy subjects and 8 glioma patients, respectively. Gray matter is abbreviated as GM and white matter is abbreviated as WM. Note, that no T_2 data of healthy subjects was available.

5 Discussion

In this work, an analysis pipeline based on existing toolboxes was implemented in MATLAB, which automatically calculates skull-stripped quantitative PD, R_1, R_2^* and T_2 parameter maps from multiple MR images with different contrast weightings. This pipeline was used to analyse the PD, R_1, R_2^*, and T_2 values in brain tissue of eight glioma patients by comparing them with a healthy cohort of five subjects and by comparing the non-affected with the affected hemisphere of each patient.
The pipeline was programmed in a modular structure, such that it can easily be adapted for other data processing pipelines in the future. For instance, the sorting of DICOM files and subsequent conversion into NIfTI format can be included into any future pipeline, as most post-processing and analysis of MR images is based on data in the NIfTI format.
The quantitative evaluation with different configuration settings showed that the absence of MT files had the largest effect on the estimated PD and R_2^* maps, while R_1 maps remained relatively unaffected. This is not surprising, as the MT files are used to improve the robustness of the fit of the exponential decay, which is used to estimate R_2^* and to extrapolate TE=0 to estimate PD [39]. However, also the choice of the operation system, the SPM version, and the rescale factor had a non-neglegible influence on the PD maps. The influence of such system and software dependent deviations is an important factor in evaluating quantitative MRI, which aims to estimate reproducible and system independet values. This evaluation showed, that even the choice of software tools used in a pipeline to analyse identical volumes can lead to considerable deviations. Further work should evaluate the influence of each parameter on the final quantitative maps more systematically.
The validation of quantitative values in five healthy subjects was performed by comparing them with values found in literature. Apart from R_2^* values, and proton densities in gray matter, the values found in this study are well within the range reported in literature ([14], [18], [31], [32], [35], [42], and [47]), which can be seen in the figures in Chapter 4.3. The deviation of proton densities in gray matter from reported literature values was rather small and can be traced back to partial volume effects. Partial volume effects occur, when the resolution is not high enough, and thus, cause the signal in a voxel to actually resemble the weighted sum of multiple tissues. However, the discrepancy between the estimated R_2^* values and reported literature values is relatively large. Apart from partial volume effects, R_2^* mapping can particularly be confounded by the presence of inomogeneities in the main magnetic field, also known as macroscopic magnetic background gradients. These macroscopic

magnetic inhomogenities introduce additional dephasing, leading to a faster signal decay, i.e. shorter T_2^*. These effects introduce systematic errors into the resulting R_2^* maps [13]. As can be seen in Figure 4.8, this assumption coincides with the observed values, as $R_2^* = 1/T_2^*$ is systematically larger than the values reported in the literature. The reason for these systematic errors is that the multi-parametric mapping protocol introduced by Weiskopf et al. [44] and used in the hMRI toolbox is not optimal to map R_2^*, as it does not correct for these macroscopic magnetic inhomogenities. Furthermore, the gray matter and white matter VOIs used for extraction of quantitative parameter values, contained brain areas at the bottom of the brain, where large magnetic field inhomogeneities occur at the borders between tissue, bone and air. The reason for the relatively broad range of 'quantitative values' in the literature is, that quantification or measurement is always accompanied by measurement errors. These measurement errors depend on the technique used for measuring; the more complex the measurement problem, the higher the error and the more the errors depend on the measurement technique. In addition, when measuring any quantitative values in human subjects, there is always an intersubject variability. Humans vary in body size, weight, and blood pressure, and most likely also in T_1 values etc. of their brain tissue.
Finally, eight glioma patients were analysed using the implemented pipeline. Since the images of the glioma patients were acquired postoperatively, the glioma itself could not be analysed. Instead, the oedema surrounding the glioma was segmented using BraTS orchestra [16] and the brain was manually split into an affected and a non-affected hemisphere, to be analysed separately.
The results vary across the investigated quantitative parameters. In general, a higher variance of values could be observed in both hemispheres of glioma patients compared to healthy subjects. This can especially be seen for the R_1 values in Figure 4.7. Although the values in both hemispheres of the patients barely differ from each other, the R_1 values of the patient cohort seems to be clustered into two distinct groups. While the first group has R_1 values comparable to healthy subjects, the second group has significant lower R_1 values, which is visible even in such a small cohort. This deviation might reflect the infiltration of tumor in surrounding tissue and indicate a further progress of disease or a different subtype of glioma. Further work with more patients is required to investigate this finding further and evaluate if R_1 can be used as a potential biomarker to detect progression of disease early on.
Other quantitative values do not suggest such a straightforward interpretation. For three patients, the PD values in gray matter coincide with healthy subjects in the non-affected hemisphere, while the corresponding PD values in the affected hemisphere deviate from each other. This might indicate potential infiltration of the glioma into the affected hemisphere, while the non-affected hemisphere still remains uninfluenced by the tumor. However, the values still lie within the range of reported literature values and the patient cohort is too small for further interpretations. Similarly, it can be observed that in some patients the R_2^* values in gray matter differ noticeable

between both hemispheres and in white matter the R_2^* values are slightly increased in the affected hemisphere. Clearly, more data of glioma patients is needed to consolidate these trends.
The analysis of T_2 was limited to the comparison between both hemispheres in patients, as no T_2 data of healthy subjects was available. No substantial differences between both hemispheres could be observed. The quantitative values in the oedema have the highest variance and differ a lot from the quantitative values both in gray and white matter. This is likely due to the higher fraction of fluid in the oedema. Only the R_1 values in the oedema seem to coincide well with R_1 values in the gray matter.

6 Conclusion

The results of this work suggest some promising trends in quantitative MRI of glioma patients which need to be investigated further in subsequent studies. The pipeline described, implemented, and validated in this work provides an ideal means to pursue patient studies with a larger subject cohort more easily and systematically. Besides further analysis of glioma patients and the search for potential biomarkes to distinguish between various types of glioma, the introduced pipeline can be utilized to investigate any type of disease that causes structural tissue changes in the brain.

Bibliography

1. M. Abramowitz and I.A. Stegun. *Handbook of mathematical functions with formulas, graphs, and mathematical tables*. US Government printing office, New York, 1964.

2. J. Ashburner and K.J. Friston. Unified segmentation. In *Neuroimage*, 26(3), pp. 839–51, 2005.

3. S. Bakas, M. Reyes, A. Jakab, S. Bauer, M. Rempfler, A. Crimi, R.T. Shinohara, C. Berger et al.. Identifying the best machine learning algorithms for brain tumor segmentation, progression assessment, and overall survival prediction in the brats challenge. https://arxiv.org/abs/1811.02629, 2018. Accessed: 23.02.2020.

4. D. Barazany, P.J. Basser, and Y. Assaf. In vivo measurement of axon diameter distribution in the corpus callosum of rat brain. In *Brain*, 132(5), pp. 1210–20, 2009.

5. F. Bloch, W.W. Hansen, and M. Packard. Nuclear induction. In *Physical Review*, 69(3-4), pp. 127–127, 1946.

6. G.B. Chavhan, P.S. Babyn, B. Thomas, M.M. Shroff, and E.M. Haacke. Principles, techniques, and applications of t2*-based mr imaging and its speical applications. In *RadioGraphics*, 29, pp. 1433–1449, 2009.

7. Digital Imaging and Communications in Medicine (DICOM). Digital imaging and communications in medicine (dicom) documentation. `https://www.dicomstandard.org/current/`. Accessed: 15.01.2020.

8. R.R. Ernst and W.A. Anderson. Application of fourier transform spectroscopy to magnetic resonance. In *Review of Scientific Instruments*, 37(1), pp. 93–102, 1966.

9. N.K. Focke, G. Helms, S. Kaspar, C. Diederich, V. Tóth, P. Dechent, A. Mohr, and W. Paulus. Multi-site voxel-based morphometry—not quite there yet. In *Neuroimage*, 56(3), pp. 1164–1170, 2011.

10. C.D. Good, I.S. Johnsrude, J. Ashburner, R.N. Henson, K.J. Friston, and R.S. Frackowiak. A voxel-based morphometric study of ageing in 465 normal adult human brains. In *Neuroimage*, 14(1), pp. 21–36, 2001.

11. S. Gutteridge, C. Ramanathan, and R. Bowtell. Mapping the absolute value of m0 using dipolar field effects. In *Magn Reson Med*, 47(5), pp. 871–9, 2002.

12. G. Helms, H. Dathe, and P. Dechent. Quantitative flash mri at 3t using a rational approximation of the ernst equation. In *Magn Reson Med*, 59(3), pp. 667–72, 2008.

13. D. Hernando, K. Vigen, A. Shimakawa, and S. Reeder. R2* mapping in the presence of b0 field variations. In *Magnetic resonance in medicine*, 68, pp. 830–40, 2012.

14. N.M. Hirsch, V. Toth, A. Förschler, H. Kooijman, C. Zimmer, and C. Preibisch. Technical considerations on the validity of blood oxygenation level-dependent-based mr assessment of vascular deoxygenation. In *NMR Biomed*, 27(7), pp. 853–62, 2014.

15. H. Huhdanpaa, D.H. Hwang, G.G. Gasparian, M.T. Booker, Y. Cen, A. Lerner, O.B. Boyko, J.L. Go, P.E. Kim, A. Rajamohan, M. Law, and M.S. Shiroishi. Image coregistration: quantitative processing framework for the assessment of brain lesions. In *J Digit Imaging*, 27(3), pp. 369–79, 2014.

16. F. Kofler, C. Berger, D. Waldmannstetter, J. Lipkopva, I. Ezhov, G. Tetteh, J.S. Kirschke, C. Zimmer, B. Wiestler, and B. Menze. Brats toolkit: Translating brats brain tumor segmentation algorithms into clinical and scientific practice. In *Frontiers in Neuroscience*, (accepted) 2020. To-appear.

17. C.K. Kuhl. Current status of breast mr imaging part 2. clinical applications. In *Radiology*, 244(3), pp. 672–691, 2007.

18. R. Kumar, S. Delshad, P.M. Macey, M.A. Woo, and R.M. Harper. Development of t2-relaxation values in regional brain sites during adolescence. In *Magn Reson Imaging*, 29(2), pp. 185–93, 2011.

19. M. Larobina and L. Murino. Medical image file formats. In *J Digit Imaging*, 27(2), pp. 200–6, 2014.

20. P.C. Lauterbur. Image formation by induced local interactions: Examples employing nuclear magnetic resonance. In *Nature*, 242(5394), pp. 190–191, 1973.

21. Z.P. Liang and P.C. Lauterbur. *Principles of magnetic resonance imaging: a signal processing perspective*. IEEE Press, New York, 2000.

22. S. Lorio, T.M. Tierney, A. McDowell, O.J. Arthurs, A. Lutti, N. Weiskopf, and D.W. Carmichael. Flexible proton density (pd) mapping using multi-contrast variable flip angle (vfa) data. In *NeuroImage*, 186, pp. 464–475, 2019.

23. A. Müller, A. Jurcoane, S. Kebir, P. Ditter, F. Schrader, U. Herrlinger, T. Tzaridis, B. Mädler, H.H. Schild, M. Glas, and E. Hattingen. Quantitative t1-mapping detects cloudy-enhancing tumor compartments predicting outcome of patients with glioblastoma. In *Cancer Med*, 6(1), pp. 89–99, 2017.

24. J. Nalepa, P. Ribalta Lorenzo, M. Marcinkiewicz, B. Bobek-Billewicz, P. Wawrzyniak, M. Walczak, M. Kawulok, W. Dudzik, K. Kotowski, I. Burda, B. Machura, G. Mrukwa, P. Ulrych, and M.P. Hayball. Fully-automated deep learning-powered system for dce-mri analysis of brain tumors. In *Artificial Intelligence in Medicine*, 102(101769), pp. 1–21, 2020.

25. Neuroimaging Informatics Technology Initiative (NIFTI). Neuroimaging informatics technology initiative (nifti) documentation. `https://nifti.nimh.nih.gov/nifti-1`. Accessed: 15.01.2020.

26. U. Nöth, J. Tichy, S. Tritt, O. Bähr, R. Deichmann, and E. Hattingen. Quantitative t1 mapping indicates tumor infiltration beyond the enhancing part of glioblastomas. In *NMR Biomed*, 33, Issue 3(e4242), pp. 1–11, 2020.

27. Q.T. Ostrom, L. Bauchet, F.G. Davis, I. Deltour, J.L. Fisher, C.E. Langer, M. Pekmezci, J.A. Schwartzbaum, M.C. Turner, K.M. Walsh, M.R. Wrensch, and J.S. Barnholtz-Sloan. The epidemiology of glioma in adults: a "state of the science" review. In *Neuro Oncol*, 16(7), pp. 896–913, 2014.

28. M. Pei, T.D. Nguyen, N.D. Thimmappa, C. Salustri, F. Dong, M.A. Cooper, J. Li, M.R. Prince, and Y. Wang. Algorithm for fast monoexponential fitting based on auto-regression on linear operations (arlo) of data. In *Magnetic resonance in medicine*, 73(2), pp. 843–850, 2015.

29. C. Pierpaoli. Quantitative brain mri. In *Topics in magnetic resonance imaging : TMRI*, 21(2), p. 63, 2010.

30. R.A. Poldrack, J.A. Mumford, and T.E. Nichols. *Handbook of Functional MRI Data Analysis*. Cambridge University Press, New York, 2011.

31. C. Preibisch and R. Deichmann. Influence of rf spoiling on the stability and accuracy of t1 mapping based on spoiled flash with varying flip angles. In *Magn Reson Med*, 61(1), pp. 125–35, 2009.

32. C. Preibisch and R. Deichmann. T1 mapping using spoiled flash-epi hybrid sequences and varying flip angles. In *Magn Reson Med*, 62(1), pp. 240–6, 2009.

33. E.M. Purcell, H.C. Torrey, and R.V. Pound. Resonance absorption by nuclear magnetic moments in a solid. In *Physical Review*, 69(1-2), pp. 37–38, 1946.

34. C. Rorden and M. Brett. Stereotaxic display of brain lesions. In *Behavioural Neurology*, 12(4), pp. 191–200, 2000.

35. M. Sabati and A.A. Maudsley. Fast and high-resolution quantitative mapping of tissue water content with full brain coverage for clinically-driven studies. In *Magnetic Resonance Imaging*, 31(10), pp. 1752–1759, 2013.

36. S.M. Smith. Fast robust automated brain extraction. In *Hum Brain Mapp*, 17(3), pp. 143–55, 2002.

37. C. Studholme and D.J. Hawkes. Normalized entropy measure for multimodality image alignment. In *Proceedings of SPIE*, 3338(1), pp. 132–143, 1998.

38. M. Symms, H.R. Jäger, K. Schmierer, and T.A. Yousry. A review of structural magnetic resonance neuroimaging. In *J Neurol Neurosurg Psychiatry*, 75(9), pp. 1235–44, 2004.

39. K. Tabelow, E. Balteau, J. Ashburner, M.F. Callaghan, B. Draganski, G. Helms, F. Kherif, T. Leutritz, A. Lutti, C. Phillips, E. Reimer, L. Ruthotto, M. Seif, N. Weiskopf, G. Ziegler, and S. Mohammadi. hmri - a toolbox for quantitative mri in neuroscience and clinical research. In *Neuroimage*, 194, pp. 191–210, 2019.

40. E.J.R. van Beek, C. Kuhl, Y. Anzai, P. Desmond, R.L. Ehman, Q. Gong, G. Gold, V. Gulani, M. Hall-Craggs, T. Leiner, C.C.T. Lim, J.G. Pipe, S. Reeder, C. Reinhold, M. Smits, D.K. Sodickson, C. Tempany, H.A. Vargas, and M. Wang. Value of mri in medicine: More than just another test? In *J Magn Reson Imaging*, 49(7), pp. 14–25, 2019.

41. J.E. Villanueva-Meyer, M.C. Mabray, and S. Cha. Current clinical brain tumor imaging. In *Neurosurgery*, 81(3), pp. 397–415, 2017.

42. J.P. Wansapura, S.K. Holland, R.S. Dunn, and W.S. Ball Jr. Nmr relaxation times in the human brain at 3.0 tesla. In *Journal of Magnetic Resonance Imaging*, 9(4), pp. 531–538, 1999.

43. D. Weishaupt, V.D. Köchli, and B. Marincek. *How does MRI work?: an introduction to the physics and function of magnetic resonance imaging*. Springer-Verlag Berlin Heidelberg, Berlin Heidelberg, 2006.

44. N. Weiskopf and G. Helms. Multi-parameter mapping of the human brain at 1mm resolution in less than 20 minutes. In *Proceedings of ISMRM*, volume 16, p. 2241. Citeseer, 2008.

45. N. Weiskopf, S. Mohammadi, A. Lutti, and M.F. Callaghan. Advances in mri-based computational neuroanatomy: from morphometry to in-vivo histology. In *Curr Opin Neurol*, 28(4), pp. 313–22, 2015.

46. N. Weiskopf, M.F. Callaghan, O. Josephs, A. Lutti, and S. Mohammadi. Estimating the apparent transverse relaxation time (r2*) from images with different contrasts (estatics) reduces motion artifacts. In *Frontiers in Neuroscience*, 8(278), pp. 1–10, 2014.

47. N. Weiskopf, J. Suckling, G. Williams, M.M. Correia, B. Inkster, R. Tait, C. Ooi, E.T. Bullmore, and A. Lutti. Quantitative multi-parameter mapping of r1, pd*, mt, and r2* at 3t: a multi-center validation. In *Frontiers in Neuroscience*, 7(95), pp. 1–11, 2013.

48. B. Wiestler, A. Kluge, M. Lukas, J. Gempt, F. Ringel, J. Schlegel, B. Meyer, C. Zimmer, S. Förster, T. Pyka, and C. Preibisch. Multiparametric mri-based differentiation of who grade ii/iii glioma and who grade iv glioblastoma. In *Sci Rep*, 6(35142), pp. 1–6, 2016.

49. M.W. Woolrich, S. Jbabdi, B. Patenaude, M. Chappell, S. Makni, T. Behrens, C. Beckmann, M. Jenkinson, and S.M. Smith. Bayesian analysis of neuroimaging data in fsl. In *NeuroImage*, 45(1, Supplement 1), pp. 173–186, 2009.

50. V.L. Yarnykh. Actual flip-angle imaging in the pulsed steady state: a method for rapid three-dimensional mapping of the transmitted radiofrequency field. In *Magn Reson Med*, 57(1), pp. 192–200, 2007.

51. R.J. Zatorre, R.D. Fields, and H. Johansen-Berg. Plasticity in gray and white: neuroimaging changes in brain structure during learning. In *Nat Neurosci*, 15(4), pp. 528–36, 2012.